Large-Eddy Simulation of flameless combustion with neural-network driven chemistry

Huu-Tri Nguyen, Camille Barnaud, Pascale Domingo, Phuc-Danh Nguyen, Luc Vervisch

Applications in Energy and Combustion Science 14 (2023) 100126

Contents lists available at ScienceDirect

Applications in Energy and Combustion Science

journal homepage: www.elsevier.com/locate/jaecs

Large-Eddy Simulation of flameless combustion with neural-network driven chemistry

Huu-Tri Nguyen [a,b], Camille Barnaud [a], Pascale Domingo [a,*], Phuc-Danh Nguyen [b], Luc Vervisch [a]

[a] CORIA – CNRS, Normandie Université, INSA Rouen Normandie, 76801 Saint-Etienne-du-Rouvray, France
[b] ArcelorMittal Global Research and Development, 57280 Maizières-lès-Metz, France

ARTICLE INFO

Keywords:
Flameless combustion
Turbulent combustion modeling
Large eddy simulation
Detailed chemistry reduction
Neural network

ABSTRACT

Large eddy simulation of a flameless combustion furnace is discussed with comparison against experimental measurements of the mean thermochemical quantities. The focus is on the introduction in flow simulations of complex chemistry through the training of neural networks, in order to simulate the oxidation of a gaseous fuel representative of recycled gases available in the steel industry. A canonical problem, based on a non-adiabatic stochastic micro-mixing model and combined with a detailed description of chemistry, is setup to train the neural networks prior to the flow simulation. For these networks to be predictive, the thermochemical composition space is decomposed into sub-domains from a partitioning algorithm. A neural network is trained in every sub-domain to return the increments in time of the most influential thermochemical quantities, from the knowledge of temperature and species mass fractions solved with the flow. Implemented in an open-source low-Mach number fluid mechanics code, the neural networks complex chemistry is shown to be very efficient in terms of CPU time, with an overhead of only 60% compared to the non-reactive multi-species simulation of the furnace.

1. Introduction

In the challenging context of decarbonization of the energy production and of the transformation industries, fuel efficiency goes along with more stringent regulation on emissions, such as NOx and particulate. To reach these objectives, actions are taken to benefit from every single opportunity regarding the recycling of any type of Low Carbon Fuel (LCF) gases produced on-site or by external parties. Thereby, many industrial combustion systems are currently revisited. In terms of burner design, multi-fuel injection stands as a promising way to transform recycled gases into additional useful energy. For instance in the steel industry, LCF includes auto-produced by-product steel gases (Coke Oven Gas (COG), Blast Furnace Gas (BFG), Basic Oxygen Furnace Gas (BOFG)), biogases and green hydrogen. Along these lines, it was discussed in the literature how the use of auto-produced steel gases can significantly reduce the environmental impact and contribute to energy saving [1,2].

For these applications, burnt gases diluted combustion and flameless oxidation appear as promising techniques to transform and benefit from residual gases. Hence, among the technologies developed for mitigating emissions from furnaces and boilers, highly diluted combustion and the so-called flameless regime have received much attention over the past twenty years, first in studies to understand the fundamentals [3–5] and then towards various applications for energy production [6,7].

The design of these combustion systems relies on both experimental and numerical simulation studies. In the present work, we discuss a strategy to account for a complex description of combustion chemistry in unsteady simulations using artificial neural networks (ANN). The objective is to benefit from a method allowing for performing multiple simulations to optimize burners and boilers, thanks to a CPU time kept to a minimum after training a set of neural networks to process the expensive time integration of the stiff chemical system of equations.

Indeed, machine learning is now a standard ingredient of computational combustion [11]. It is used for building sub-models from various databases used to train neural networks (including DNS or canonical problems) or to reduce CPU time by replacing specific costly numerical operations performed during the solving of the aerothermochemical equations. Pioneer works in the field have discussed an integrated probability density function/neural network approach for simulating turbulent reacting systems [12]. Artificial neural networks were also used in the 90's to model the temporal evolution of reduced combustion chemistry [13]. More recently, tabulation of chemistry via ANN was addressed [14]. A skeletal mechanism was derived with neural networks in order to simulate a laminar jet diffusion flame of

* Corresponding author.
E-mail address: pascale.domingo@insa-rouen.fr (P. Domingo).

https://doi.org/10.1016/j.jaecs.2023.100126
Received 10 August 2022; Received in revised form 16 November 2022; Accepted 22 February 2023
Available online 2 March 2023

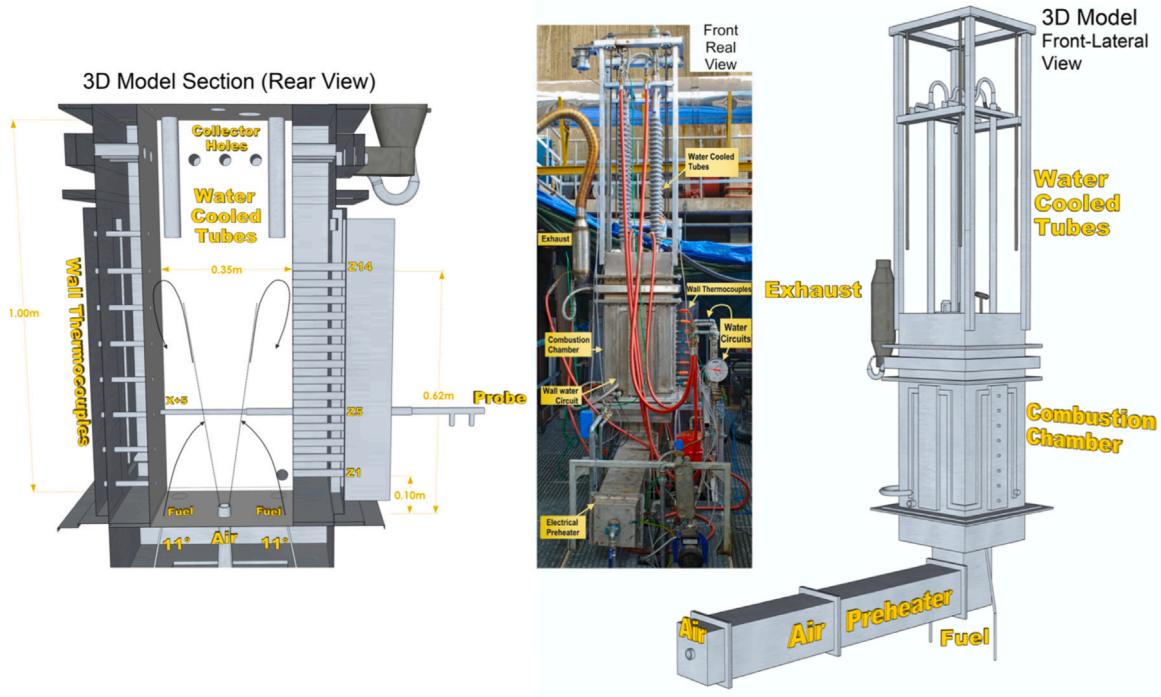

Fig. 1. Schematic and picture of the UMONS furnace [8–10] (Lengths in m).

Table 1
UMONS inlet conditions.

Inlet	B50	Air	Recirculation
X_{CH_4} (molar fraction)	0.1425	–	–
X_{H_2}	0.325	–	–
X_{N_2}	0.28	0.79	0.696219
X_{O_2}	–	0.21	0.0175578
X_{CO_2}	0.12	–	0.112496
X_{CO}	0.1325	–	–
X_{H_2O}	–	–	0.173727
T(K)	290.65	1075.66	1300
Mass flow rate (kg/s)	0.002572941	0.010293228	0.064330844
Reynolds number	22400	19600	–
Bulk velocity (m/s)	98	65	–
Pressure (Pa)	101325	101325	101325

methly formate [15] and ANN based chemical mechanisms proposed for modeling hydrogen/carbon monoxide/kerosene combustion [16]. Deep ANNs have been applied to multi-dimensional flamelet libraries and spray flames [17] and an ANN based hybrid chemistry framework was discussed [18]. Chemistry reduction using machine learning trained from non-premixed micro-mixing modeling was applied to syngas turbulent oxy-combustion [19] and an on-the-fly ANN chemistry procedure was proposed for direct numerical simulation [20]. The population balance equation for soot was also solved using ANN [21].

On the sub-grid scale modeling side, neural network-based closure have been evaluated for the unresolved stresses in turbulent premixed V-flame [22]. A generic framework was discussed for data-based turbulent combustion closure and tested a posteriori [23]. Progress variable variance and filtered rate modeling have been studied using convolutional neural networks and flamelet methods [24]. The direct mapping from LES resolved scales to filtered-flame generated manifolds was achieved with convolutional neural networks [25]. Other convolutional neural networks were introduced to classify combustion modes and secure monitoring of supersonic combustion [26]. Deep learning was shown efficient to perform super-resolution reconstruction of turbulent flows [27]. Raman/Rayleigh line measurements were combined with machine learning for combustion regime identification [28]. Reduced-order models based on principal component analysis allowed for developing digital twins for various reactive flow applications [29]. Reactive flow solvers have also been developed from machine learning [30] and much more works addressing turbulent combustion modeling may be found in above references.

The partially-stirred reactor (PaSR) generic concept was introduced in large variety of formulations in the literature for simulating highly diluted combustion. PaSR were for instance used to study the effect of hydrogen on H_2/CH_4 flame structure of MILD combustion [31] and to simulate H_2/N_2 lifted flame in a vitiated co-flow [32] or to describe a piloted lean premixed jet flame with finite-rate chemistry [33]. The Eddy Dissipation Concept was also extended to model turbulence/chemistry interactions in MILD combustion [34] and to study the reactive structures of NOx emissions of methane/hydrogen mixtures in flameless combustion [35]. The influence of kinetic uncertainties on the accuracy of numerical modeling of an industrial flameless furnace fired with NH_3/H_2 blend was addressed in a combined experimental and numerical study [36,37], also examining the role of mixing models in MILD combustion [38]. The specific aspect of internal recirculation and how it impacts on modeling accuracy was carefully examined [39] along with strategies for hydrogen-enriched methane flameless combustion [40].

Here we start by devising a procedure to build, from a detailed chemical combustion kinetics, a database representative of the thermochemical conditions which can be expected in a flameless furnace. The method relies on stochastic micro-mixing, including the specific high-dilution rates and heat-losses as observed in the UMONS furnace studied experimentally [8–10]. From this database, a set of neural networks are trained to return the increment in species mass fractions and temperature for a given thermochemical state. These networks are then introduced in a Large-Eddy Simulation (LES) flow solver to be combined with a simple formulation of turbulence/chemistry interaction modeling, in order to simulate the furnace and results are compared against experimental measurements.

The subsequent section reports on the flow configuration, the numerical methods and turbulence modeling. After that, the focus is on the structures of the networks and their training in view of combustion chemistry integration in LES. The training database is presented and verified, with a discussion on the compromise between multiplying the

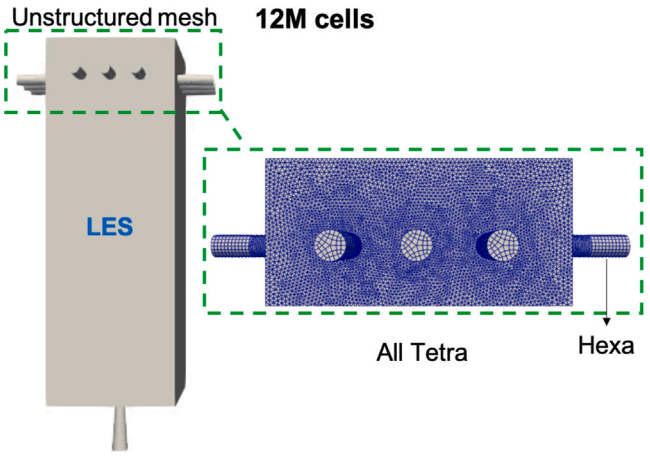

Fig. 2. UMONS furnace configuration and mesh.

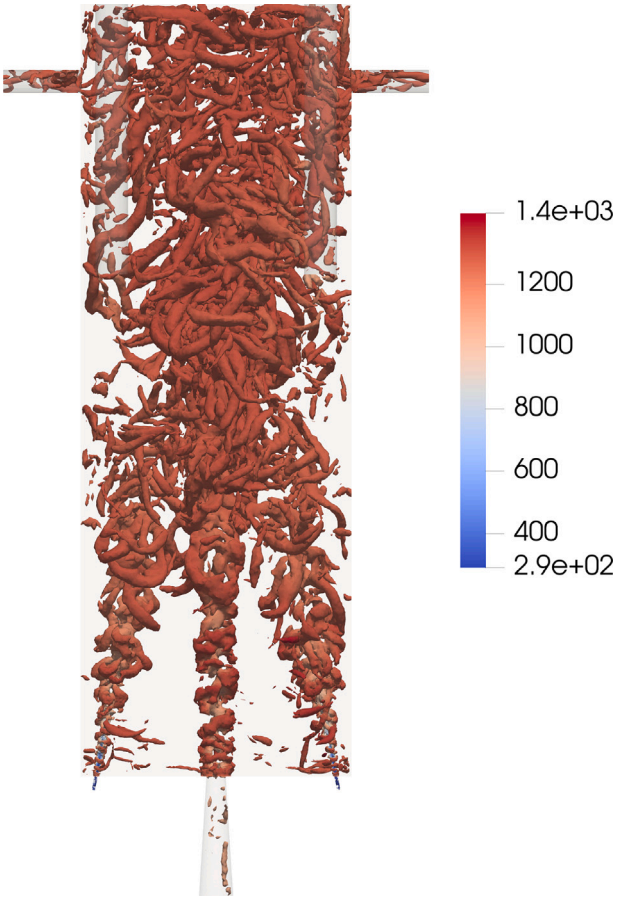

Fig. 3. Instantaneous iso-surface of Q criterion [41]. $Q = 6.10^5\ s^{-2}$, colored by temperature in Kelvin.

number of both, the heat loss levels and the amount of dilution by burnt gases, and, the simple application of data blurring, to benefit from accurate predictions. Finally, the statistics obtained from LES are compared against measurements before concluding.

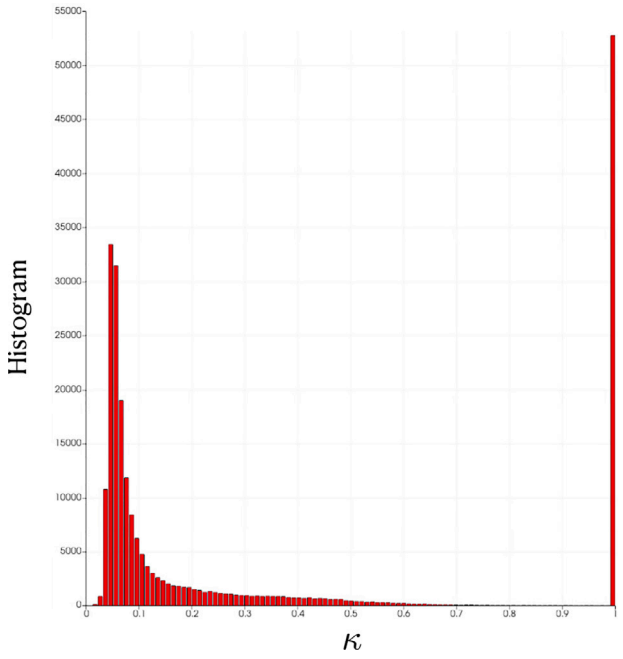

Fig. 4. Histogram of the values of κ (Eq. (2)).

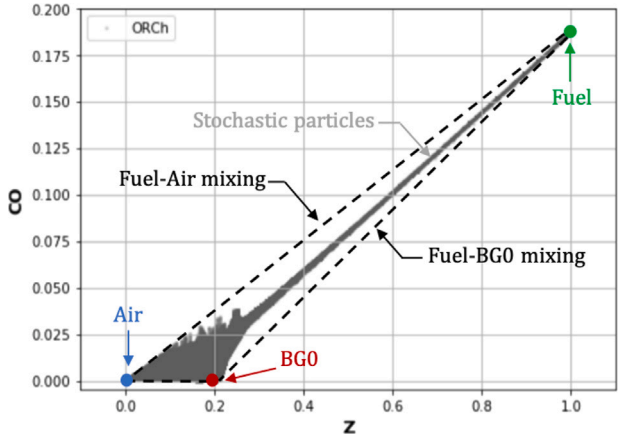

Fig. 5. CO stochastic particles mass fraction versus mixture fraction (gray dots). BG0: Burnt gases inlet. Fuel: B50 gas inlet (Table 1).

2. Reactive flow configuration and numerics

2.1. UMONS flameless furnace

The UMONS lab-scale furnace [8–10] is a 30 kW pilot experiment operating under the flameless combustion mode, hence with high dilution of the fresh reactants (air and fuel) by burnt gases and strong heat transfer to a thermal charge, with radiative transfer contributing to about 80% of the total heat transfer. This lab-scale furnace was designed to mimic some of the main features of industrial furnaces, through the configuration of the injection of the gases, the global geometry of the enclosure, the amount of air preheating and the variable thermal charge.

The combustion chamber is made of stainless steel and it is equipped with a fibrous ceramic heat insulation layer. It consists of a square inner section of 0.35 m × 0.35 m for 1.0 m high (Fig. 1). A single air injection lies in the center of the bottom wall. Two gas injectors with 11° tilt angle are symmetrically located around this air injector.

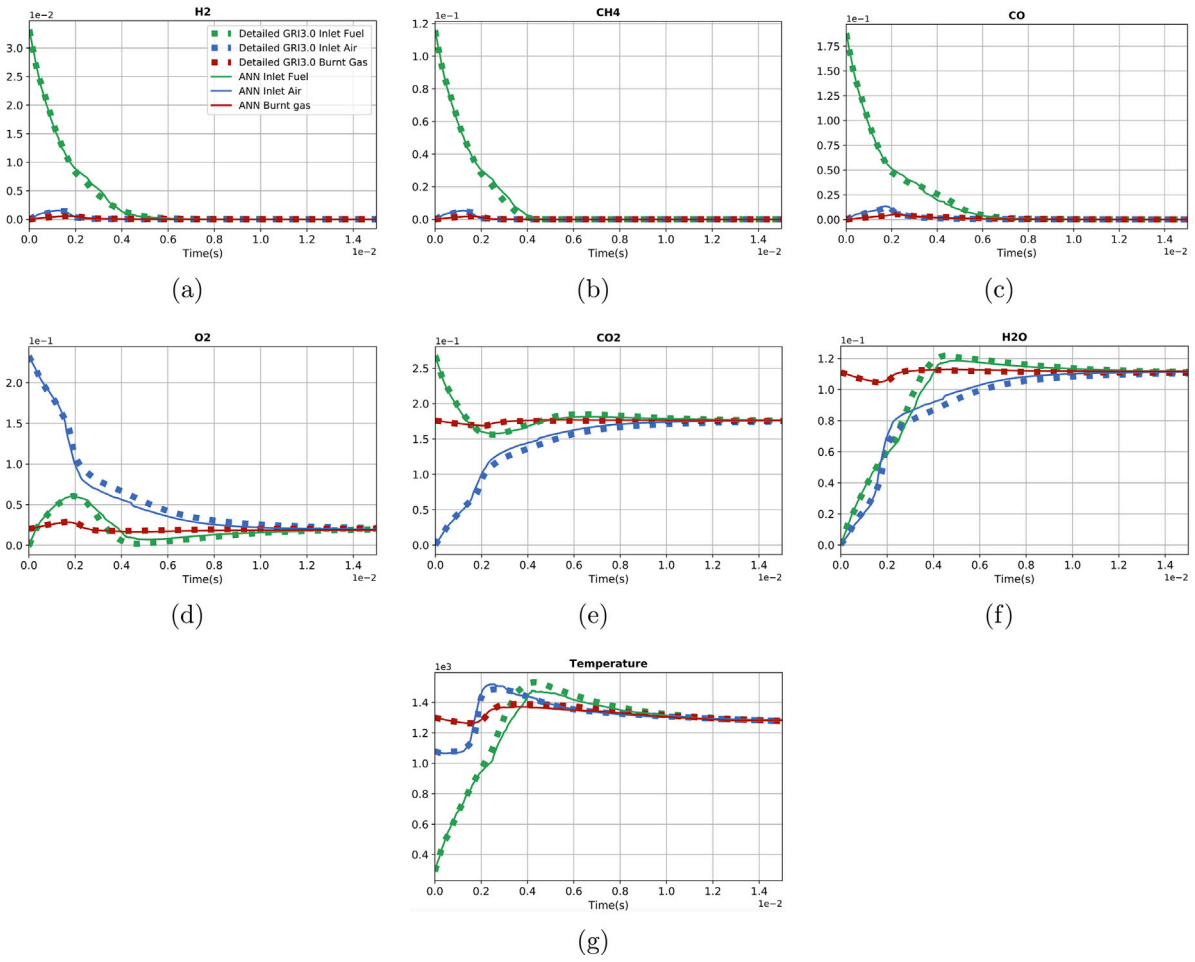

Fig. 6. Time evolution of major species mass fraction and temperature in Kelvin averaged over stochastic particles with $\alpha_{loss} = 3 \cdot 10^5$ and time step of $5 \cdot 10^{-7}$ s. Symbols: detailed chemistry. Line: ANN.

The air is preheated up to 1000 °C by an electrical system and the fuel, named B50, is composed of 50% in volume of representative coke-oven gas (COG) and low calorific blast-furnace gas (BFG) of heating value 10.3 MJ/Nm^3, the overall equivalence ratio is 0.89, see Table 1 summarizing gases composition and inlet mass flow rates. The composition of the recirculating burnt gases is taken at the outlet of the furnace, also in agreement with recent Reynolds averaged simulations [10]. The mass flow rate of the recirculation inlet is calculated from the dilution rate which is equal to 5. The thermal charge and the furnace temperature are controlled through four water cooling tubes (heat sink) whose immersion can be regulated from 0 to 90 cm. A reduced water circuit is also added along the outer walls. According to the measurements, this thermal charge extracts about 60% of combustion heat release, 80% of which by radiative heat transfer and 20% by convection [10]. Each vertical wall of the combustion chamber has a removable part. A wall (on the rear side) is equipped with a quartz window to allow for optical access and image recording. A side wall (on the right) is equipped with eight S-type thermocouples, separated from each other by 9 cm and mounted flush with the insulation layer, to provide a wall temperature profile along the furnace height in the vertical symmetry plane containing the air and gas injectors. Probes are also inserted inside the furnace through fourteen holes on the wall opposite to the thermocouples wall, to measure the temperature and species concentration of O_2, CH_4, CO_2 and CO (on dry basis) by paramagnetic and infrared gas analysers. Measurement of H_2 and N_2 and additional measurements of O_2, CH_4 and CO were realized by a gas chromatograph. More details regarding the experimental procedure can be found in the literature [8,10,42,43].

2.2. Flow solver and modeling

The Navier–Stokes equations (momentum, energy and species mass fractions) are solved using the open source software Code_Saturne [44]. It relies on a co-located second order accurate cell-centered finite volume approach operating over unstructured grids. The full volume of the furnace is meshed, including the 12 exhaust cylinders, with a non-uniform mesh of 12 million cells, featuring tetrahedrons and hexahedrons (Fig. 2). On the bottom wall where gases are injected, the mesh is so that y^+ is just below unity, while $7 < y^+ < 15$ on the lateral walls. The mesh is strongly refined in the shear layers developing downstream of jet injection with a resolution down to 0.2 mm. From previous RANS simulations [10], the integral length scales in the shear layers are about 10 mm and 5 mm in the air and the gas jets. The resolution is thus adequate to capture the large scale flow motions and the corresponding kinetic energy they contain. Fig. 3 shows the vortical structures which develop from the three jets, to then be combined and merge further downstream, they are colored by the temperature. At the bottom close to injections, the reactants are mixed with recirculating burnt products trapped between the jets, while the temperature is indeed almost uniform as expected in the flameless combustion regime.

2.2.1. Turbulence-chemistry interaction modeling

Combustion in systems where reactants are injected through separated jets, thus operating in the non-premixed mode, is overall controlled by a partial mixing of the reactants occurring at large and medium flow length scales, followed by micro-mixing and molecular diffusion at smaller scales, where reactants are put in contact and

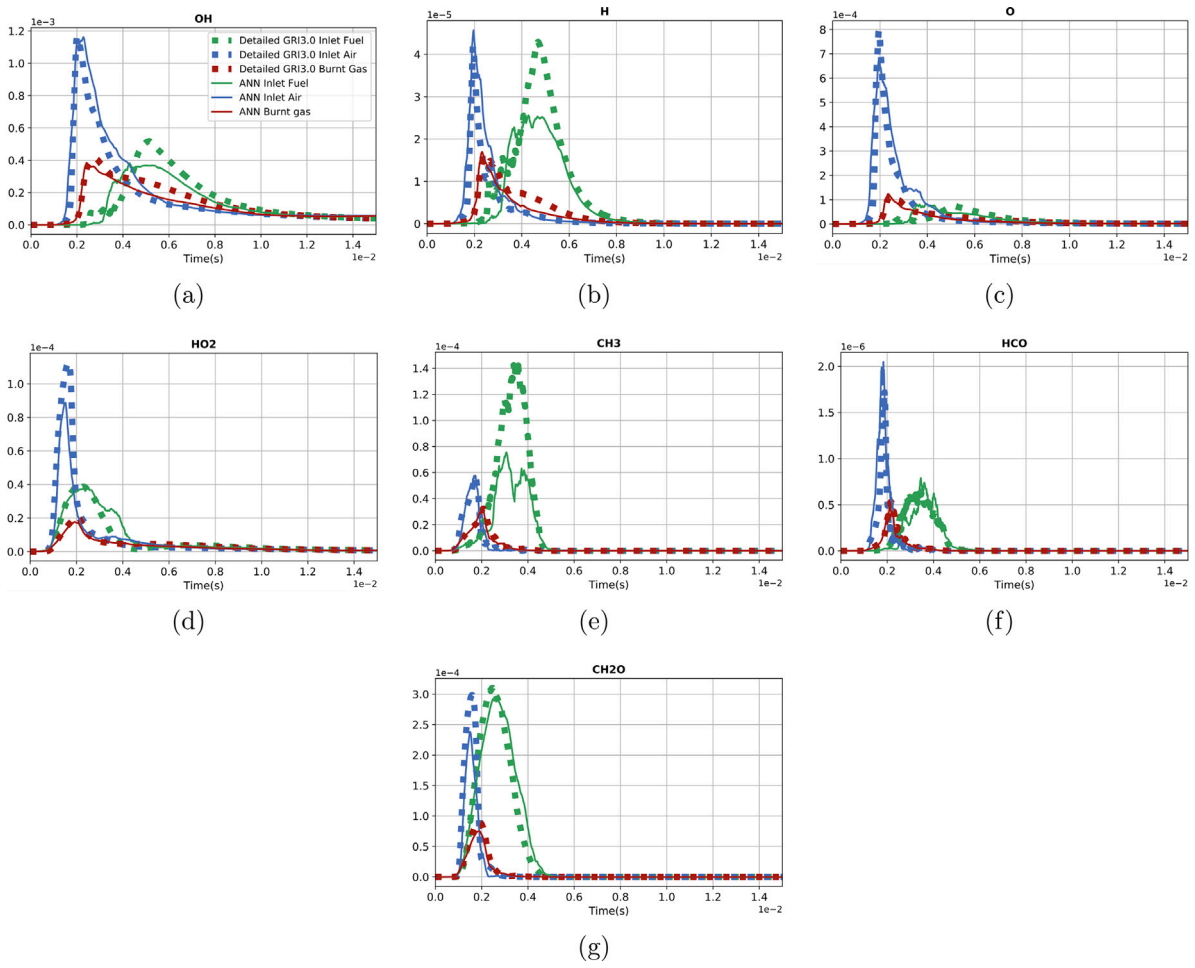

Fig. 7. Time evolution of minor species mass fraction averaged over stochastic particles with $\alpha_{loss} = 3 \cdot 10^5$ and time step of $5 \cdot 10^{-7}$ s. Symbols: detailed chemistry. Line: ANN.

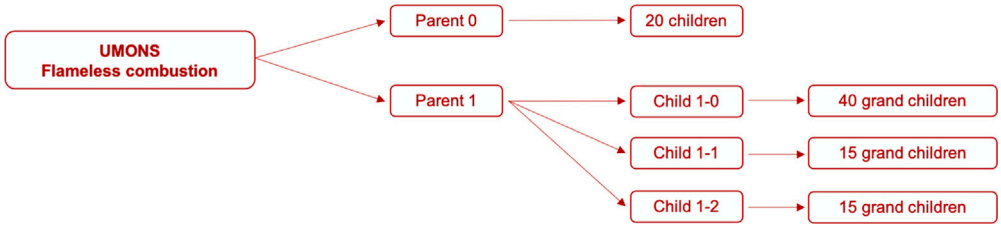

Fig. 8. Schematic of the decomposition in clusters for ANN training.

chemical reactions occur [45]. Depending on the range of flow and chemical characteristic time scales at play, finite rate chemistry and other small-scales aero-thermochemical processes can strongly influence the operation of such furnace [5]. However, because the highly diluted combustion regime goes with quite homogeneous mixture and because the filtered thermochemical quantities are here resolved with a mesh of about 200 µm in the reaction zones, scalars feature very weak gradients away from the injection zones. Sub-grid scale scalar fluctuations are then neglected at first to compute a reference chemical source directly from the resolved field. In a second step, as in [46] this source is modulated through a sub-grid Damköhler number, essentially to account for the fast mixing occurring in the vicinity of the injection of the reactants, fast mixing which can locally slowdown chemistry.

$\overline{\dot{\omega}}_k$ denotes the LES filtered burning rate (or volume averaged over the mesh cell), which enters the balance equation for the kth thermochemical quantity. $\dot{\omega}_k(\widetilde{\underline{Y}}, \widetilde{T})$ is the burning rate computed from quantities resolved by the mesh, where $\widetilde{\underline{Y}}$ and $\widetilde{T}$ are the LES filtered vector of mass fractions and temperature respectively. $\dot{\omega}_k(\widetilde{\underline{Y}}, \widetilde{T})$ is weighted by the reacting fraction κ [47], so that the filtered burning rate reads

$$\overline{\dot{\omega}}_k = \kappa \dot{\omega}_k(\widetilde{\underline{Y}}, \widetilde{T}) \,. \tag{1}$$

The faster the chemistry (i.e. the smaller the chemical time t_c), the larger $\dot{\omega}_k(\widetilde{\underline{Y}}, \widetilde{T})$. However, in each computational cell, the reacting fraction κ must decrease if $t_{\mathrm{m},\Delta}$, the mechanical mixing time in the cell of characteristic size Δ, becomes larger than the chemical time, since mixing is then not fast enough to fully feed the reactions occurring at the smallest turbulent flow scales. Hence, $\kappa = \overline{\dot{\omega}}_k / \dot{\omega}_k(\widetilde{\underline{Y}}, \widetilde{T})$ is assumed to be proportional to the ratio of characteristic times representative of t_c the reaction time and of $t_c + t_{\mathrm{m},\Delta}$, the total conversion time in the computation cell, defined as the sum of the reaction time and the sub-grid scale mixing time ($t_{\mathrm{m},\Delta}$) [47]:

$$\kappa = \frac{t_c}{t_c + t_{\mathrm{m},\Delta}} = \frac{1}{1 + Da_m} \,, \tag{2}$$

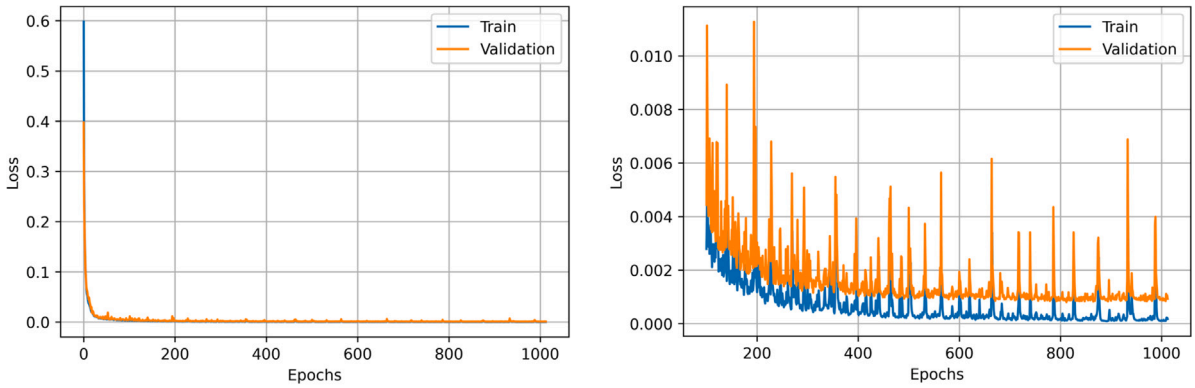

Fig. 9. Time evolution of the loss function.

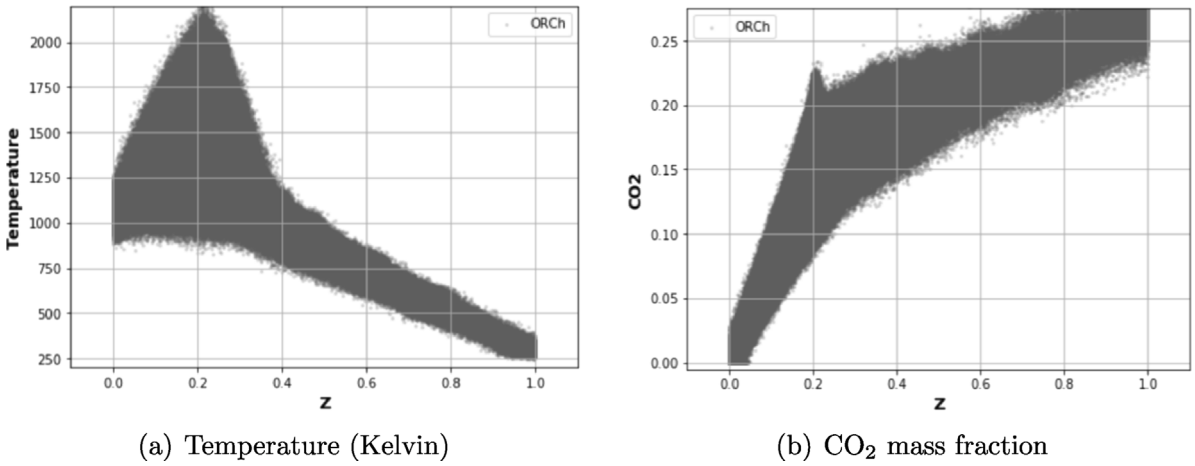

Fig. 10. State diagram of stochastic particles in mixture fraction space for a noised case.

where the sub-grid Damköhler number $Da_m = t_{\mathrm{m},\Delta}/t_{\mathrm{c}}$ has been introduced. Because of the very weak gradients of all the thermochemical quantities which are almost uniform, after ignition the characteristic chemical time do not vary too much. In practice, it is whether the mixture is ignited or not that overall drives the process and using a single chemical time based on ignition to define t_c was found sufficient to obtain satisfying results. Here $t_c = 5.10^{-6}$ s is the shortest representative ignition delay of the mixture for the present operating conditions, as observed in the detailed chemistry simulation reported thereafter. The mechanical mixing time $t_{m,\Delta}$ is approximated from the Smagorinksy SGS model [48,49], used in the simulations to represent transport by unresolved velocity fluctuations:

$$t_{m,\Delta} = \frac{(C_s\Delta)^2}{\nu + \nu_{sgs}}\,. \tag{3}$$

C_s is the parameter of the dynamic procedure [50] applied to approximate the SGS viscosity in the simulation, $\nu_T = (C_s\Delta)^2|S|$, where $|S| = (2S_{ij}S_{ij})^{1/2}$, with $S_{ij} = (\nabla\mathbf{u} + \nabla\mathbf{u}^T)/2$. $\mathbf{u}$ is the velocity vector, ν is the molecular viscosity and $\Delta = V^{\frac{1}{3}}$, with V the volume of the cell.[1] LES of MILD combustion in the same furnace was conducted for a different mixture using a formulation similar to the one used in this work [51]. Fig. 4 reports the histogram of the values of κ computed where the chemical heat release rate is non-zero. It is seen that $\kappa = 1$ dominates, with another set of points in the jet shear layers where κ values are centered around 0.1.

Within this framework, the neural networks are trained to return $\delta Y_k = \dot{\omega}_k(\widetilde{\underline{Y}}, \widetilde{T}) \times \delta t$, where δt denotes the time-step. During time iterations in the flow solver, convection and diffusion are first solved, then the increment due to chemistry is directly read from the networks. Sub-iterations may be required in case the time-step is larger in the flow solver than during the training phase of the network.

2.2.2. Radiative heat transfer modeling

The weighted-sum-of-gray-gases (WSGG) approach is applied to model radiative heat transfer [52]. The emissivity weighting factors and absorption coefficients of combustion products (H_2O and CO_2) are calculated using correlations [53]. Three gray gases are considered to minimize CPU time and memory requirements [10,54]. The discrete ordinate method (DOM-S_4, 24 directions) [55,56] is used to discretize the radiative transfer equation (RTE) over the three-dimensional mesh.

3. ANN reduced chemistry for flameless combustion

3.1. Training database

The strategy for building the neural networks training database relies on previous works [19,57]. Stochastic micromixing modeling is combined with complex chemistry to generate, prior to any flow simulation, the variety of thermochemical conditions expected in the combustion system. In this approach, the fraction of flow rate injected through a given inlet defines the number of stochastic particles taking

[1] Notice that this formulation for the chemical source would not be valid in Reynolds averaged context (RANS), there it would be mandatory to account for unresolved fluctuations of scalars when estimating the chemical source.

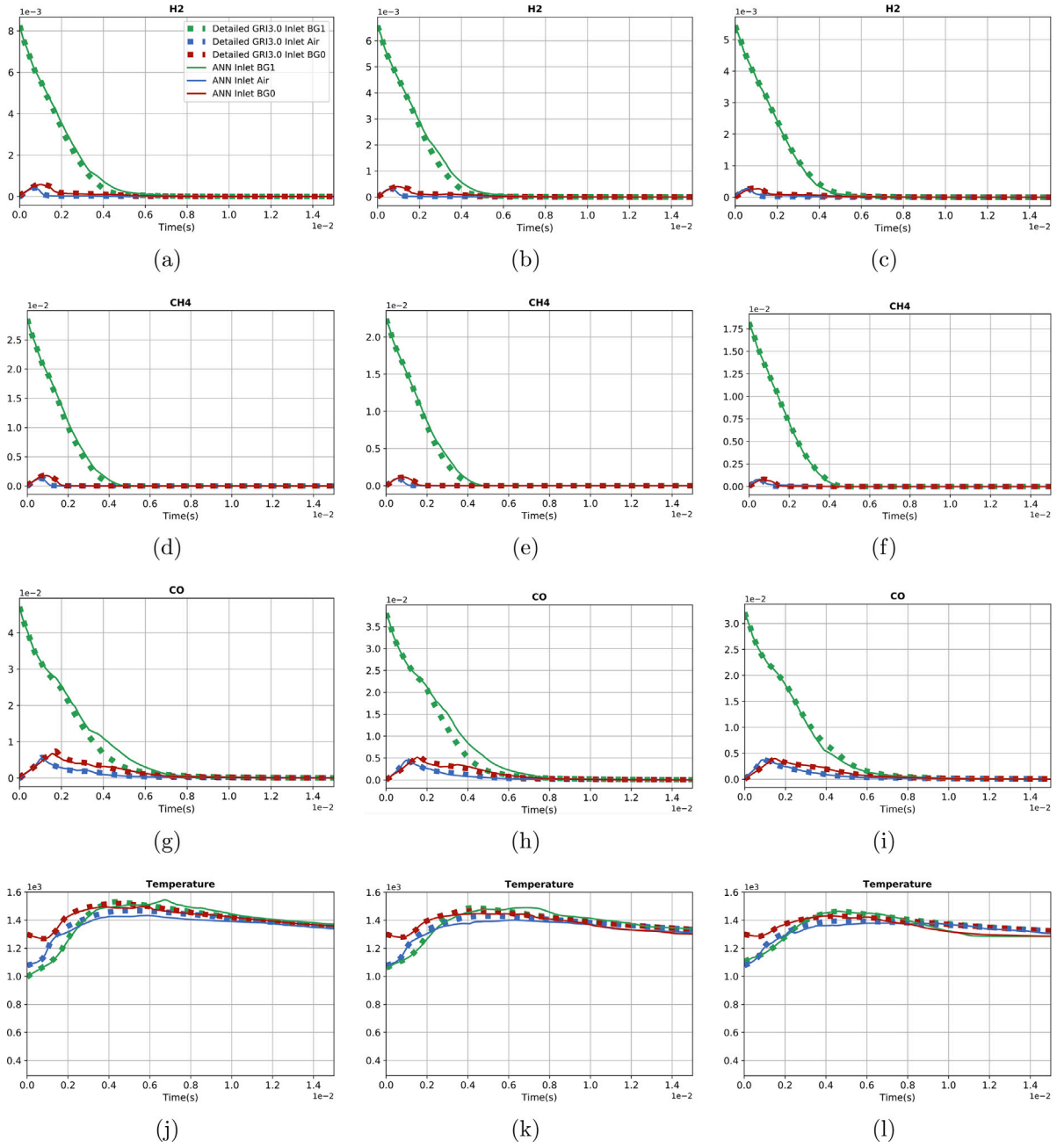

Fig. 11. Time evolution of major species mass fraction and temperature in Kelvin averaged over stochastic particles with $\alpha_{loss} = 1.5 \cdot 10^5$ and time step of $5 \cdot 10^{-6}$ s for 3 ratios of burnt gases recirculation rate. Left: 3. Middle: 4. Right: 5.

the thermochemical properties of that inlet at initial time. Each particle carries information on the species mass fraction vector and enthalpy. From this non-premixed initial condition, the stochastic particles evolve in time according to[2]

$$\frac{\partial Y_k^p(t)}{\partial t} = \mathrm{MIX}^p(\tau_\mathrm{T}) + \dot{\omega}_{Y_k}^p \,, \tag{4}$$

$$\frac{\partial h_s^p(t)}{\partial t} = \mathrm{MIX}^p(\tau_\mathrm{T}) + \dot{\omega}_{h_s}^p + \alpha_{loss}(T_p - T_{wall}) \,. \tag{5}$$

$Y_k^p(t)$ is the mass fraction of the pth particule, $\mathrm{MIX}^p(\tau_\mathrm{T})$ denotes the Euclidian Minimum Spanning Tree micromixing model [60] and $\dot{\omega}_{Y_k}^p$ is the chemical source. The characteristic value of the micromixing time, $\tau_T =$ 0.3 ms, was determined from previous simulations of the furnace [10]. Varying τ_T in Eqs. (4)–(5) around its nominal value was found to have a relatively weak impact for the purpose of database generation in view of chemistry reduction, at least as long as ignition occurs [58]. To account for the non-adiabatic character of the flow, a linear heat loss term is added and calibrated with the variable coefficient α_{loss}, the temperature of the particle T_p and the average wall temperature measured in the experiments $T_{wall} = 1259.4$ K. The parameter α_{loss} is chosen so that the mean chemical equilibrium temperature of the ensemble of stochastic particles ranges between 1200 and 1500 K, as reported experimentally in the recirculating burnt gases. The first training database is then composed of three set of stochastic particles evolving from their initial condition up to equilibrium, for α_{loss} taking the values $3 \cdot 10^5$, $5 \cdot 10^5$ and $7 \cdot 10^5$ W kg^{-1} K^{-1}. Eqs. (4) and (5) are solved with routines from the Cantera package [61].

[2] Other applications of this class of model problem for chemistry reduction and process control may be found in the literature [58,59].

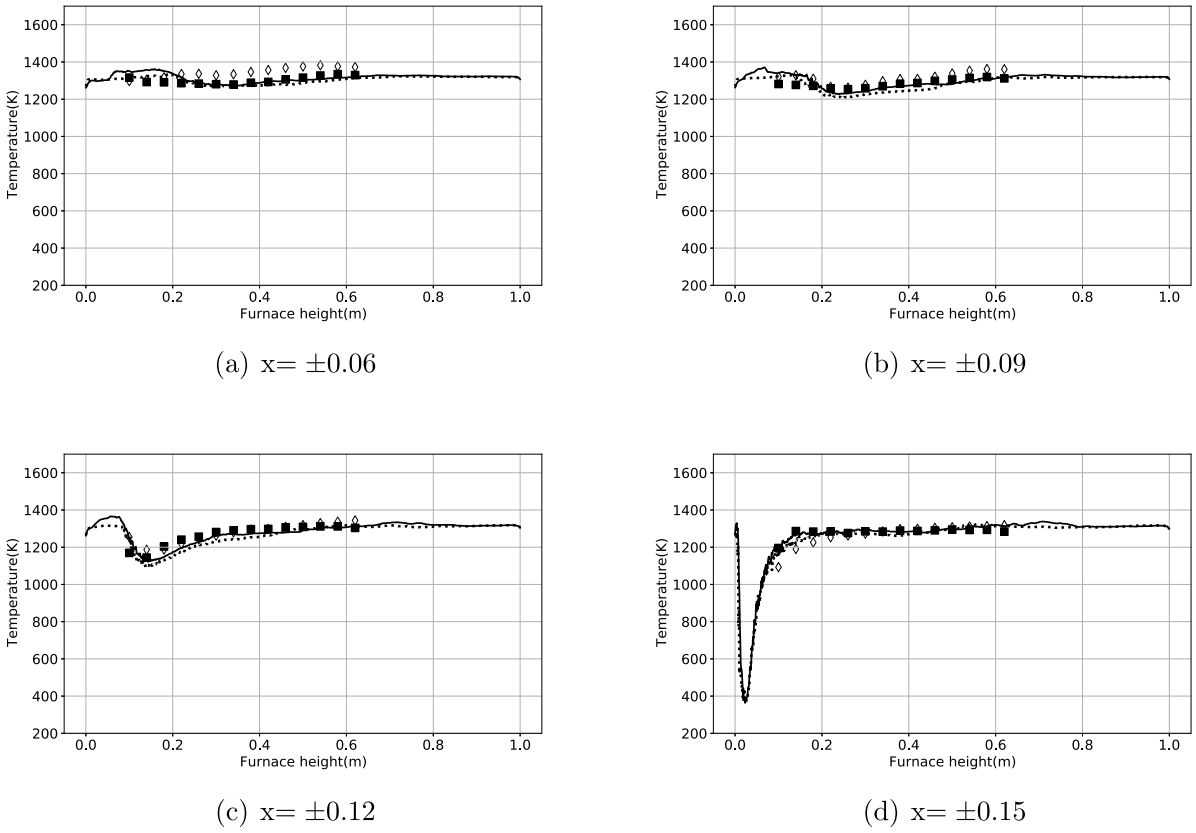

Fig. 12. Experimental (symbol) and simulated (line) vertical profiles of mean temperature in Kelvin. Dashed line and empty symbols: $x < 0$ (left side of furnace). Line and symbols: $x > 0$ (right side). Maximum measurement uncertainty is 7.6 K [42,43].

Three inlets are imposed to build every set of time evolving stochastic particles. These inlets carry respectively the B50 gas, air and a given amount of recirculating equilibrium burnt products (Table 1). This third inlet is necessary because with separated jet injection, the reactants are mixed with recirculating burnt gases before they meet and this specific behavior must be included in the training thermochemical dataset. The estimated mass flow rate of recirculating burnt gases, as provided experimentally, is given in Table 1. In practice, the system of Eqs. (4)–(5) is then solved with, at initial time, 25 stochastic particles of B50, 102 particles of air and 643 particles of recirculating burnt gases. A composition space (CO-mixture fraction) distribution of the particles representative of these conditions is shown in Fig. 5.

The time evolution of the relevant species mean mass fractions and temperature computed over the stochastic particles are shown in symbol with the GRI-3.0 detailed chemistry mechanism [62] for $\alpha_{loss} = 3.10^5$ and a time-step of 5.10^{-7} s in Fig. 6 for major species and in Fig. 7 for minor species. The identification of the species relevant to capture the thermochemistry, and whose increment in time shall be learned by the neural networks, is achieved applying the direct relation graph with error propagation analysis (DRGEP) [63] to the trajectories seen in these figures. Starting from the detailed scheme GRI3.0, 14 species were identified as essential to follow the dynamics of the chemical system evolution: H_2, H, O, O_2, OH, H_2O, HO_2, CH_3, CH_4, CO, CO_2, HCO, CH_2O and N_2. These species mass fractions and the temperature will serve as input to the neural networks, which are trained to return their increments, or source terms, for a given time step. Meaning that 14 scalars will be solved in LES.

3.2. Clustering thermochemical data and ANN structure

A single neural network cannot handle the large variety of chemical conditions seen by the gases during their evolution from injection up to chemical equilibrium. Following a previously develop approach [57], the dataset is first decomposed in clusters and a dedicated neural network will be affected to every cluster. Multiplying the numbers of ANN to secure precision does not increase significantly the CPU time of the flow simulation, as all the ANNs are implemented as subroutines in the computational fluid dynamics (CFD) solver and called according to the thermochemical composition space location of the mesh cell to be advanced in time. However, this considerably impacts on the CPU devoted to training, as discussed in the next subsection.

The decomposition of the dataset into subdomains implies the application of pre-treatments, such as centering, rescaling and clustering with K-means. [64]. More precisely, we use the K-means++ algorithm [65], which stands as a well-established unsupervised machine learning algorithm to group similar data into different clusters. The algorithm assigns randomly a first centroid, a second centroid is then chosen as farthest as possible to the first centroid, a third centroid is as farthest as possible to the first two centroids, and so on. Then, every data point is assigned to the cluster with the shortest Euclidean distance in the multi-dimensional composition space. The centroid locations are updated by averaging all data points in each cluster and the process is repeated until the centroid locations are converged by evaluating the shifting tolerance which is chosen at 10^{-20}.

There is a general trend of combustion data to cluster simply in two groups according to fresh and burnt gases. Also to refine the analysis, a hierarchical clustering strategy is adopted [57]. The first clustering separates fresh and burnt gases (Parent 0 and Parent 1 in Fig. 8). The Parent 0 cumulates the data from mixing, ignition and combustion stages, it is further decomposed into 20 child clusters. The data subset in the second parent, representing the final stage of combustion up to the ultimate equilibrium state, was found to require a special treatment in the case of flameless combustion in order to guarantee the success of ANN training. This second parent is decomposed into only 3 child

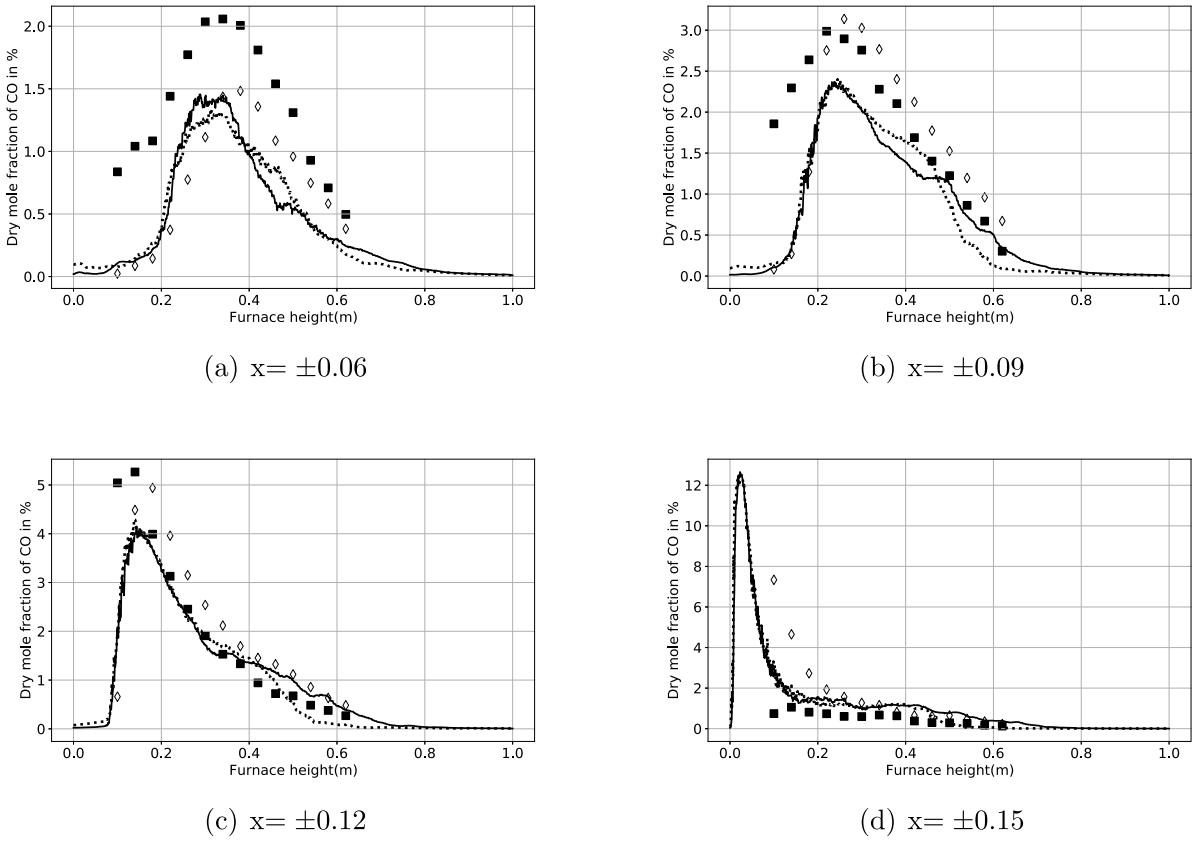

Fig. 13. Experimental (symbol) and simulated vertical profiles of mean CO in volume percentage on dry basis. Dashed line and empty symbols: $x < 0$ (left side of furnace). Line and symbols: $x > 0$ (right side). Maximum measurement uncertainty is 0.28%.

Table 2
Structure of ANNs [19].

Layer	Output shape	Activation function
Input	(None, 11)	–
Dense	(None, 512)	ReLU
Dense	(None, 256)	ReLU
Dense	(None, 128)	ReLU
Dense	(None, 64)	ReLU
Dense (Output)	(None, 11)	–

clusters, which will have respectively, 40, 15 and 15 grandchildren. Each child cluster of the first parent and each grandchild cluster of the second parent benefits from its own ANN training. During LES, from the input state vector composed of the species mass fractions and temperature, the Euclidean distance to each cluster centroid is calculated. The LES mesh point is then assigned to the cluster located at the minimum distance.

The ANN regression structure (Table 2) is similar to previous works [19] (Table 2). Every ANN consists of 1 input layer, 4 dense hidden layers with the rectified linear activation function (ReLU) and 1 output layer. The total number of parameters (weights and biases) is 179851. The database is split into training set (81%), validation set (9%) and test set (10%) for model verification. The training is performed for a fixed time-step of $5 \cdot 10^{-7}$ s.

The training process is performed using Tensorflow 2 with GPU support (NVIDIA GeForce GTX 1080 Ti) and the Adam optimizer in default setting. To avoid overfitting, the early stopping callback is used and set as 200 epochs. The check point callback saves the best model with the lowest mean squared error (MSE) during the training process. The parameters of the default setting of the Tensorflow 2 Adam optimizer are used with a learning rate set at 0.001. The training- and validation-loss were found to diverge, also the check point call back procedure was introduced to avoid overfitting. The 200 epochs were chosen to ensure that the final trained model always has the lowest validation loss. The training curves are shown in Fig. 9. The overall training, validation and test errors are within the range $[10^{-5}, 10^{-3}]$. (Beside early stopping callback, the dropout method was also tested but it did not show significant impact and the training process took longer.)

3.3. ANNs verification and database blurring

The ANNs are trained to return the increments, or source terms, for the species mass fractions and temperature, knowing the vector of species mass fractions and temperature (ANN input). To verify the quality of the training, the evolution of the stochastic particles is simulated again from Eqs. (4) and (5), but replacing the computation of the chemical sources from the detailed mechanisms by the ANNs output.

The strategy reported in previous works [19] is applied to fully insure mass conservation after the removal of the less influential species. The mass imbalance in the source of atom A is measured for reduced set of species

$$\Delta\dot{\omega}_{\mathrm{A}} = \sum_{i=1}^{N_s^r} \frac{\beta_{\mathrm{A},i} W_{\mathrm{A}}}{W_i} \dot{\omega}_i \,, \tag{6}$$

where W_{A} and W_i are molar weights and $\beta_{\mathrm{A},i}$ the number of atom 'A' in the ith species. Sources of carbon containing species and of hydrogen containing species are corrected adding

$$\Delta\dot{w}_i = -\frac{Y_i}{Y_{\mathrm{A}}} \Delta\dot{\omega}_{\mathrm{A}} \,, \tag{7}$$

with the atom mass fraction $Y_{\mathrm{A}} = \sum_{i=1}^{N_s^r} \beta_{\mathrm{A},i}(W_A/W_i)Y_i$. For oxygen, Eq. (7) is applied only to O_2 and with the already corrected sources of C and H containing species.

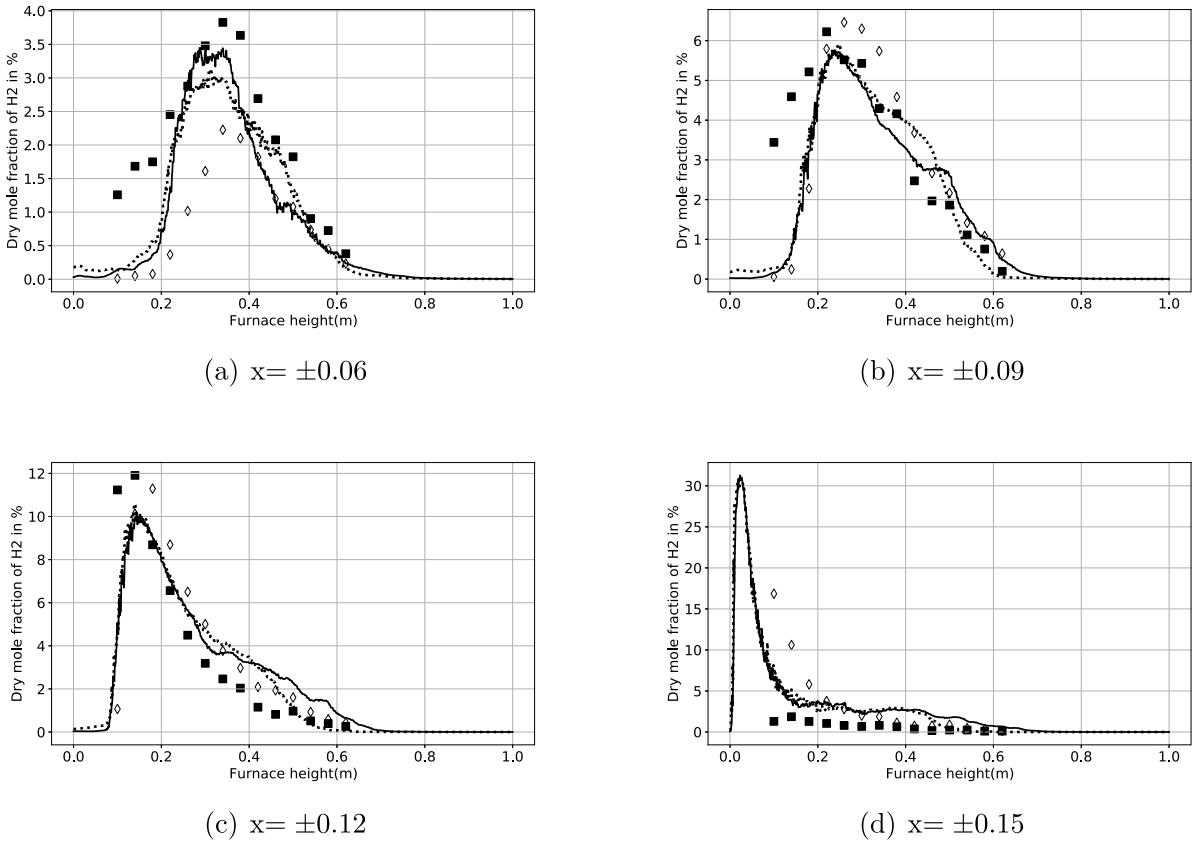

Fig. 14. Experimental (symbol) and simulated vertical profiles of mean H_2 in volume percentage on dry basis. Dashed line and empty symbols: $x < 0$ (left side of furnace). Line and symbols: $x > 0$ (right side). Maximum measurement uncertainty is 0.72%.

Comparing in Figs. 6 and 7 the time evolution of the major and minor species, results are quite convincing. Some departure exists for the minor species, but it is acceptable considering the strong reduction of the number of species transported, here from 53 to 14. Computing these evolutions is 80 times faster with the ANN than integrating the detailed chemistry, notice that this speed-up would depend on the stiffness of the detailed chemistry. Once the overall procedure setup has been verified for the micromixing canonical problem, it is extended to address the UMONS furnace test case.

As a matter of fact, within the UMONS furnace, the diversity of the thermochemical conditions are more pronounced than those generated by the canonical problem reported above. One of the major issue lies in the huge variability in the amount of burnt gases locally mixed with the reactants, mainly because the recirculation rate of burnt products is far from being uniform in space. The fuel may for instance be mixed only with burnt gases without air within coherent flow structures, which are then convected quite far downstream before meeting air. (See Figs. 11 and 12).

A successful attempt was made to extend the above database by considering additional levels of burnt gases recirculation, i.e., varying the amount of stochastic particles within the third inlet of the model problem (Eqs. (4)–(5)). However, these additional levels coupled together with the different heat-loss levels lead to a computing effort for training which rapidly became prohibitive.

Following previous works in which the control of database augmentation combined with improvement in training efficiency was achieved from a systematic blurring [19,21,25], 5% of Gaussian noise is added to all variables in all cases of the above dataset, still conserving mass thanks to Eqs. (6)–(7). The final database contains 25.238.581 rows. The training is performed following the very same procedure reported above but in parallel using 8 GPUs (NVIDIA Tesla K80) and it is completed in about 7 h runtime.

Fig. 10 shows the temperature and CO_2 responses in mixture fraction space for the noised database. Following the same procedure as above, the ANNs obtained with this noised database are verified by solving Eqs. (4) and (5) with detailed and ANN-based chemistry. For this test, three dilutions ratios are considered (ratio between burnt gases mass flow rate and sum of fuel and air mass flow rates) and with a lower level of heat-loss $\alpha_{loss} = 1.5 \cdot 10^5$, in order to mimic different conditions. The trained ANNs capture quite well the thermochemical response, as seen in Fig. 11.

4. Results and comparison against measurements

Fig. 12 shows the comparison between measured and computed averaged temperature. The rather flat temperature profiles expected in a flameless combustion regime are observed. The temperature field is quasi-homogeneous in the simulation, without hot spots representative of thin flame reaction zones. Both locations on the left side ($x < 0$) and on the right side ($x > 0$) of the furnace are displayed. At the locations of x = ±0.12 m and ±0.15 m, the measured temperature decreases in the vicinity of the fuel jet, a trend that is well recovered by the simulations.

The distributions of the three species, CO, H_2 and CH_4, initially present in the fuel and produced/consumed by combustion, are compared against measurements in Figs. 13–15. Results are also convincing. The peak values in the profiles correspond to the fuel jet. The measured species profiles at the location of x = ±0.15 m (Figs. 13(d), 14(d) and 15(d)) feature a significant asymmetry between the right and left sides, while the numerical results show rather similar profiles on both sides. Thereby, the computed species profiles agree with the measured species profile at x = −0.15 m, but not at x = +0.15 m. According to these experimental profiles at x = +0.15 m, the molar fractions of CO, H_2 and CH_4 stays very low in the vicinity of the fuel jet on the side of positive abscissa (the right side of the furnace), where the sampling

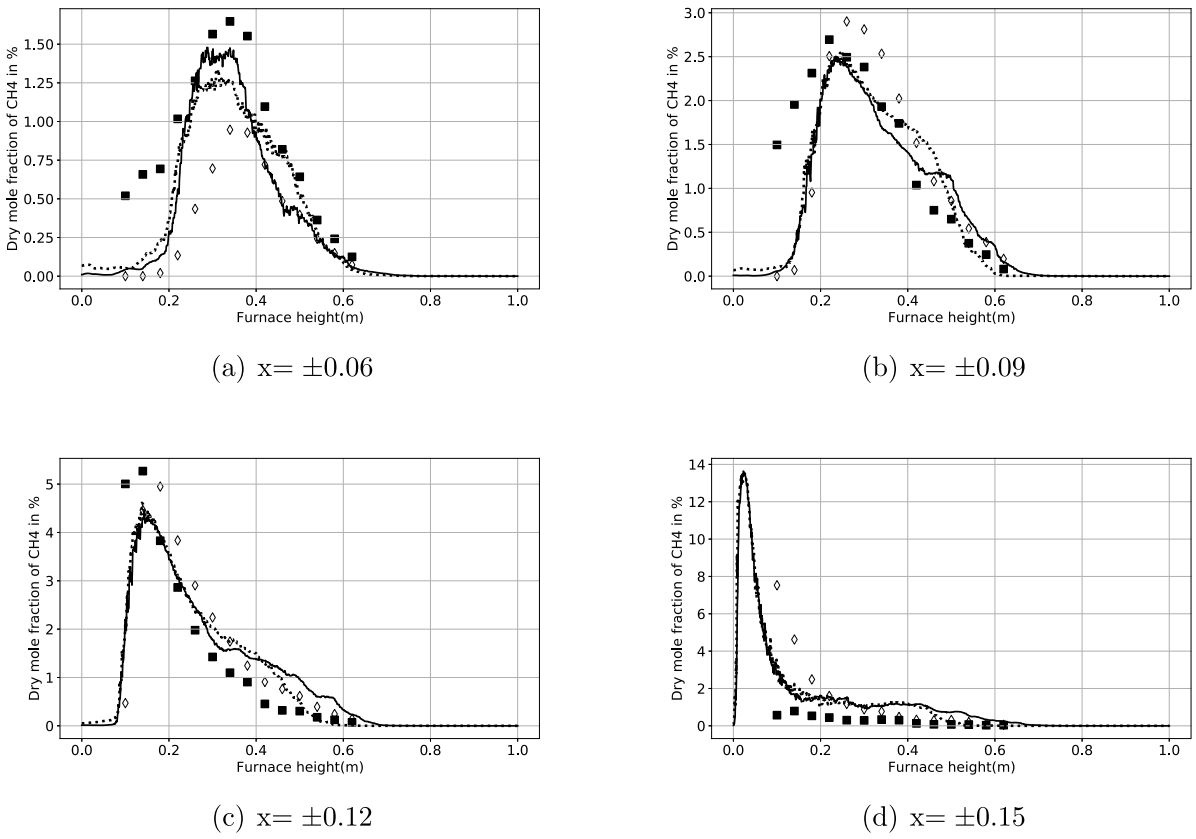

Fig. 15. Experimental (symbol) and simulated vertical profiles of mean CH_4 in volume percentage on dry basis. Dashed line and empty symbols: $x < 0$ (left side of furnace). Line and symbols: $x > 0$ (right side). Maximum measurement uncertainty is 0.27%.

probe was introduced. It is therefore likely that the discrepancy in the measurements between the two sides results from spurious perturbation by the probe.

Overall the CPU cost of the simulation with the ANN chemistry solver is only 1.6 times the CPU cost of the simulation of the variable density flow within the furnace without chemistry, thus opening many perspectives for the application of LES to such industrial combustion systems.

5. Conclusion

Neural networks have been introduced in large-eddy simulation of a flameless combustion furnace [42,43] to speed up the time integration of chemistry. Storing the species mass fraction increments, the neural networks both reduce and pre-integrate stiff chemical systems. In a low-Mach number flow solver, with time-splitting for chemistry, the neural networks directly return the updated state of the thermochemical parameters, allowing for performing the complex chemistry simulations at a very moderate CPU cost.

To achieve the ANN training prior to the flow simulation, a stochastic micro-mixing model problem with heat-loss and dilution by burnt gases is simulated with a detailed chemical scheme. It is shown that an acceptable level of accuracy can be achieved after clustering the data in the thermochemical composition space applying standard machine learning tools. A family of neural networks, each dedicated to a given cluster, are finally trained to be applied in the simulations. The CPU increase from a non-reactive multi-species simulation (i.e., from a reference simulation transporting the 14 species for convection and diffusion) is of only 60% with chemistry solved with ANN.

The numerical results compare well with experiments, which is very encouraging considering the low computing cost of these simulations. However, to fully conclude on the validity and the robustness of this approach, additional test cases need to be considered, also including measurements of emissions such as NOx or particulate, to further develop and consolidate the modeling. Indeed, a simplified description of the turbulence chemistry interaction (TCI) has been used to focus on the CPU gain brought by the introduction of ANNs. The TCI modeling part of the work could be improved by developing machine learning based closures specialized in combustion regimes where reactants are highly diluted by recirculating burnt products.

Declaration of competing interest

The authors declare that they have no known competing financial interests or personal relationships that could have appeared to influence the work reported in this paper.

Data availability

Data will be made available on request.

Acknowledgments

The Ph.D. of the first author is funded by ANRT (Agence Nationale de la Recherche et de la Technology), France and ArcelorMittal, France under the CIFRE No. 2019/0056. This work is also supported by ADEME (Agence de l'Environnement et de la Maîtrise de l'Energie), France under the project IGAR (Injection de Gaz de Recycle) Grant Nb 1882C001. Computing resources were provided by CRIANN (http://www.criann.fr).

References

[1] Nguyen PD, Ghazal G, Piñera VC, Battaglia V, Rensgard A, Ekman T, et al. Modelling of flameless oxy-fuel combustion with emphasis on radiative heat transfer for low calorific value blast furnace gas. Energy Procedia 2017;120:492–9.

[2] Cuervo-Piñera V, Cifrián-Riesgo D, Nguyen P-D, Battaglia V, Fantuzzi M, Della Rocca A, et al. Blast furnace gas based combustion systems in steel reheating furnaces. Energy Procedia 2017;120:357–64.

[3] Wünning JA, Wünning JG. Flameless oxidation to reduce thermal NO-formation. Prog Energy Combust Sci 1997;23:81–94.

[4] Hasegawa T, Tanaka R. High temperature air combustion-revolution in combustion technology; Part I: New findings on high temperature air combustion. JSME Int J Ser B 1998;41:1079–84.

[5] Cavaliere A, de. Joannon M. Mild combustion. Prog Energy Combust Sci 2004;30:329–66.

[6] Perpignan AAV, Gangoli Rao A, Roekaerts DJEM. Flameless combustion and its potential towards gas turbines. Prog Energy Combust Sci 2018;69:28–62.

[7] Hosseini S. Fundamentals of low emission flameless combustion and its applications. 1st ed.. Academic Press; 2022, p. 598.

[8] Mosca G. Experimental and numerical study on MILD combustion of low LHV fuels (Ph.D. thesis), Polytech de Mons; 2017.

[9] Mosca G, Lupant D, Lybaert P. Effect of increasing load on the MILD combustion of COG and its blend in a 30 kW furnace using low air preheating temperature. Energy Procedia 2017;120:262–9.

[10] Nguyen P-D, Nguyen H-T, Domingo P, Vervisch L, Mosca G, Gazdallah M, et al. Flameless combustion of low calorific value gases, experiments and simulations with advanced radiative heat transfer modeling. Phys Fluids 2022;34:045123.

[11] Ihme M, Chung WT, Mishra AA. Combustion machine learning: Principles, progress and prospects. Prog Energy Combust Sci 2022;91(101010).

[12] Christo F, Masri A, Nebot E, Pope S. An integrated PDF/neural network approach for simulating turbulent reacting systems. Symp (Int) Combust 1996;26(1):43–8.

[13] Blasco JA, Fueyo N, Dopazo C, Ballester J. Modelling the temporal evolution of a reduced combustion chemical system with artificial neural network. Combust Flame 1998;113(1–2):38–52.

[14] Franke LL, Chatzopoulos AK, Rigopoulos S. Tabulation of combustion chemistry via Artificial Neural Networks (ANNs): Methodology and application to LES-PDF simulation of Sydney flame L. Combust Flame 2017;185:245–60.

[15] Padilha FRR, Bortoli ALD. Solutions for a laminar jet diffusion flame of methly formate using a skeletal mechanism obtained by applying ANNs. J Math Chem 2019;57:2229–47.

[16] An J, He G, Luo K, Qin F, Liu B. Artificial neural network based chemical mechanisms for computationally efficient modeling of hydrogen/carbon monoxide/kerosene combustion. Int J Hydrogen Energy 2020;45(53):29594–605.

[17] Owoyele O, Kundu P, Ameen MM, Echekki T, Som S. Application of deep artificial neural networks to multi-dimensional flamelet libraries and spray flames. Int J Engine Res 2020;21(1):151–68.

[18] Ranade R, Alqahtani S, Farooq A, Echekki T. An ANN based hybrid chemistry framework for complex fuels. Fuel 2019;241:625–36.

[19] Wan K, Barnaud C, Vervisch L, Domingo P. Chemistry reduction using machine learning trained from non-premixed micro-mixing modeling: Application to DNS of a syngas turbulent oxy-flame with side-wall effects. Combust Flame 2020;220:119–29.

[20] Chi C, Janiga G, Thévenin D. On-the-fly artificial neural network for chemical kinetics in direct numerical simulations of premixed combustion. Combust Flame 2021;226:467–77.

[21] Seltz A, Domingo P, Vervisch L. Solving the population balance equation for non-inertial particles dynamics using PDF and neural networks: Application to a sooting flame. Phys Fluids 2021;33(013311).

[22] Nikolaou ZM, Chrysostomou C, Minamoto Y, Vervisch L. Evaluation of a neural network-based closure for the unresolved stresses in turbulent premixed V-flames. Flow Turbul Combust 2021;106(2):331–56.

[23] Ranade R, Echekki T. A framework for data-based turbulent combustion closure: A posteriori validation. Combust Flame 2019;210:279–91.

[24] Nikolaou Z, Chrysostomou C, Vervisch L, Cant RS. Progress variable variance and filtered rate modelling using convolutional neural networks and flamelet methods. Flow Turbul Combust 2019;103(2):485–501.

[25] Seltz A, Domingo P, Vervisch L, Nikolaou ZM. Direct mapping from LES resolved scales to filtered-flame generated manifolds using convolutional neural networks. Combust Flame 2019;210:71–82.

[26] Zhu X, Cai Z, Wu J, Cheng Y, Huang Q. Convolutional neural network based combustion mode classification for condition monitoring in the supersonic combustor. Acta Astronaut 2019;159:349–57.

[27] Liu B, Tang J, Huang H, Lu X-Y. Deep learning methods for super-resolution reconstruction of turbulent flows. Phys Fluids 2020;32:025105.

[28] Wan K, Hartl S, Vervisch L, Domingo P, Barlow R, Hasse C. Combustion regime identification from machine learning trained by Raman/Rayleigh line measurements. Combust Flame 2020;219:168–274.

[29] Aversano G, Bellemans A, Li Z, Coussement A, Gicquel O, Parente A. Application of reduced-order models based on PCA & Kriging for the development of digital twins of reacting flow applications. Comput Chem Eng 2019;121(2):422–41.

[30] An J, Wang H, Liu B, Luo KH, Qin F, He GQ. A deep learning framework for hydrogen-fueled turbulent combustion simulation. Int J Hydrogen Energy 2020;45(35):17992–8000.

[31] Afarin Y, Tabejamaat S. Effect of hydrogen on H2/CH4 flame structure of mild combustion using the LES method. Int J Hydrogen Energy 2013;38(8):3447–58.

[32] Duwig C, Fuchs L. Large Eddy Simulation of a H2/N2 lifted flame in a vitiated co-flow. Combust Sci Technol 2008;180(3):453–80.

[33] Duwig C, Nogenmyr K-J, Chan C-K, Dunn MJ. Large Eddy Simulation of a piloted lean premixed jet flame using finite-rate chemistry. Combust Theory Model 2011;15(4):537–68.

[34] Parente A, Malik MR, Contino F, Cuoci A, Dally BB. Extension of the Eddy Dissipation Concept for turbulence/chemistry interactions to MILD combustion. Fuel 2016;163:98–111.

[35] Ferrarotti M, De Paepe W, Parente A. Reactive structures and NOx emissions of methane/hydrogen mixtures in flameless combustion. Int J Hydrogen Energy 2021;46(68):34018–45.

[36] Ferrarotti M, Bertolino A, Amaduzzi R, Parente A. On the Influence of Kinetic uncertainties on the accuracy of numerical modeling of an industrial flameless furnace fired with NH3/H2 blends: a numerical and experimental study. Front Energy Res 2020;8:597655.

[37] Ferrarotti M, Furst M, Cresci E, De Paepe W, Parente A. Key modeling aspects in the simulation of a quasi-industrial 20 kW moderate or intense low-oxygen dilution combustion chamber. Energy Fuels 2018;32(10):10228–41.

[38] Ferrarotti M, Li Z, Parente A. On the role of mixing models in the simulation of MILD combustion using finite-rate chemistry combustion models. Proc Combust Inst 2019;37(4):4531–8.

[39] Amaduzzi R, Ceriello G, Ferrarotti M, Sorrentino G, Parente A. Evaluation of modeling approaches for mild combustion systems with internal recirculation. Front Mech Eng 2020;6:20.

[40] Amaduzzi R, Ferrarotti M, Parente A. Strategies for hydrogen-enriched methane flameless combustion in a quasi-industrial furnace. Front Energy Res 2021;8:353.

[41] Hunt JCR, Wray AA, Moin P. Eddies, stream, and convergence zones in turbulent flows. In: Annual research briefs. Center for Turbulence Research, Stanford; 1988, p. 193–208.

[42] Lupant D, Pesenti B, Lybaert P. Influence of probe sampling on reacting species measurement in diluted combustion. Exp Therm Fluid Sci 2010;34(5):516–22.

[43] Lupant D, Lybaert P. Assessment of the EDC combustion model in MILD conditions with in furnace experimental data. Appl Therm Eng 2015;75:93–102.

[44] EDF. Code_Saturne V7. URL https://www.code-saturne.org/cms/web/.

[45] Bray KNC. The challenge of turbulent combustion. Symp (Int) Combust 1996;26:1–26.

[46] Wan K, Xia J, Vervisch L, Liu Y, Wang Z, Cen K. Modelling alkali metal emissions in large-eddy simulation of a preheated pulverised-coal turbulent jet flame using tabulated chemistry. Combust Theory Model 2018;22(2):203–36.

[47] Chomiak J, Karlsson A. Flame liftoff in diesel sprays. Symp (Int) Combust 1996;26(2):2557–64.

[48] Smagorinsky J. General circulation experiments with the primitives equations. Mon Weather Rev 1963;61:99–164.

[49] Sagaut P. Large eddy simulation for incompressible flows: an introduction. 2nd ed.. Berlin Heidelberg: Springer-Verlag; 2001.

[50] Germano M, Piomelli U, Moin P, Cabot W. A dynamic subgrid-scale eddy viscosity model. Phys Fluids A Fluid Dyn 1991;3:1760.

[51] Cordier M. Large eddy simulation of MILD combustion, application to free-jets and a lab-scale furnace Doctor in Engineering Sciences and Technology, UniversitÉ de Mons; 2021.

[52] Hottel H, Sarofim A. Radiative transfer. New York: McGraw-Hill; 1967.

[53] Smith T, Shen Z, Friedman J. Evaluation of coefficients for the weighted sum of gray gases model. J Heat Transfer 1982;104(4):602–8.

[54] Johansson R, Andersson K, Leckner B, Thunman H. Models for gaseous radiative heat transfer applied to oxy-fuel conditions in boilers. Int J Heat Mass Transfer 2010;53(1–3):220–30.

[55] Coelho PJ. Numerical simulation of the interaction between turbulence and radiation in reactive flows. Prog Energy Combust Sci 2007;33(4):311–83.

[56] Christo F, Dally BB. Modeling turbulent reacting jets issuing into a hot and diluted coflow. Combust Flame 2005;142(1–2):117–29.

[57] Nguyen H-T, Domingo P, Vervisch L, Nguyen P-D. Machine learning for integrating combustion chemistry in numerical simulations. Energy AI 2021;5(100082).

[58] Jaouen N, Vervisch L, Domingo P, Ribert G. Automatic reduction and optimisation of chemistry for turbulent combustion modeling: Impact of the canonical problem. Combust Flame 2017;175:60–79.

[59] Farcy B, Vervisch L, Domingo P, Perret N. Reduced-order modeling for the control of selective non-catalytic reduction (SNCR). AIChE J 2016;62(3):928–38.

[60] Subramaniam S, Pope SB. A mixing model for turbulent reactive flows based on Euclidean Minimum Spanning Trees. Combust Flame 1998;115(4):487–514.
[61] Goodwin D. Cantera: An object-oriented software toolkit for chemical kinetics, thermodynamics, and transport processes. 2009, http://code.google.com/p/cantera.
[62] Smith GP, Golden DM, Frenklach M, Moriarty NW, Eiteneer B, Goldenberg M, et al. Tech. rep., 1999, http://www.me.berkeley.edu/gri-mech/.
[63] Pepiot P, Pitsch H. An efficient error propagation based reduction method for large chemical kinetic mechanisms. Combust Flame 2008;154(1–2):67–81.
[64] MacQueen J. Some methods for classification and analysis of multivariate observations. In: Proceedings of the fifth Berkeley symposium on mathematical statistics and probability. Vol. 1. No. 14. Oakland, CA, USA; 1967, p. 281–97.
[65] Arthur D, Vassilvitskii S. K-means++: the advantages of careful seeding. Tech. rep., Stanford; 2006.